

M2R Internship

On the Variability of the Thermohaline Circulation

Elise Poupart
Supervisor: **Achim Wirth**

UMR 5519 - Laboratoire des Écoulements Géophysiques et Industriels (LEGI)
Équipe Modélisation des Écoulements Océaniques à Moyenne et grande échelle (MEOM)
Domaine Universitaire BP 53 38041 GRENOBLE Cédex 9, FRANCE

February to June 2011

Remerciements

Tout d'abord, je remercie le laboratoire LEGI pour son chaleureux accueil pendant ce stage de M2R. La sympathique équipe des thésards me laisse un très bon souvenir. Les ingénieurs de recherche Raphaël Dussin, Jean-Marc Molines et Gabriel Moreau, toujours très disponibles, m'ont été d'une grande aide lors de mes pérégrinations numériques.

Je remercie la SNCF qui, malgré sa réputation sulfureuse, n'a pas accusé trop de retard sur les trajets Lyon-Grenoble pendant la période de mon stage.

Enfin, je remercie bien sûr Achim Wirth pour sa gentillesse, sa disponibilité et sa pédagogie tout au long de ce stage qui m'a vivement intéressée et motivée.

Abstract

The thermohaline circulation is a key component of the Global Climate System, and possesses a variability on a wide range of time scales (month to millions of years). The two major drivers of the thermohaline circulation are: (i) the localized and intermittent injection by a process of vigorous deep convection at high latitudes, and (ii) the basin-wide and slowly-varying upwelling. In this study, a highly simplified dynamic model of the thermohaline circulation (Stommel Arons model) is subject to time-varying injection and upwelling.

Characteristic time-scales of the two main deep flows are determined. The rapid Deep Western Boundary Current (DWBC) dynamics is dominated by the fast injection and advective time-scales, while the deep northward interior flow is determined by the upwelling and the time-scales of the slow adjustment to the forcing done by Rossby waves.

By adding an obstacle at the western boundary, small changes are found in the Eulerian description, whereas the Lagrangian properties of the flow are considerably changed. Indeed, in the time-varying injection case, some water masses are diverted from the DWBC to the interior of the deep ocean in the vicinity of the obstacle. Once they penetrate the interior of the deep ocean, they join the deep northward interior flow. This finding explains the Grand Banks (Newfoundlands) 'paradox' between Eulerian observations of a continuous DWBC and Lagrangian buoys leaving the DWBC at the Grand Banks. Indeed, at the southern tip of the Grand Banks, almost all the buoys launched in the DWBC are ejected towards the interior of the basin, where they undergo a subsequent northward displacement, while the DWBC seems to follow a continuous pathway along the indented western boundary of the North Atlantic ocean.

La circulation thermohaline joue un rôle clé dans le Système Climatique Global, et possède une variabilité sur une large gamme d'échelles de temps (du mois jusqu'au million d'années). Les deux moteurs principaux de la circulation thermohaline sont (i) l'injection et (ii) l'upwelling. L'injection (i), ayant lieu lors de vigoureux épisodes convectifs profonds aux hautes latitudes, est intermittente et localisée. Au contraire, l'upwelling (ii) se fait dans tout le bassin et varie peu au cours du temps. Dans cette étude, un modèle dynamique de la circulation thermohaline très simple (modèle de Stommel Arons) est soumis à un forçage injection/upwelling dépendant du temps.

Les échelles de temps caractéristiques des deux principaux écoulements profonds de la circulation thermohaline sont déterminées. La dynamique rapide du Courant Profond de Bord Ouest est dominée par les courtes échelles de temps advective et de l'injection. L'écoulement vers le Nord dans l'intérieur du bassin est déterminé par l'upwelling et par les grandes échelles de temps des ondes de Rossby, intervenant dans les processus d'ajustement de la dynamique du système suite au forçage.

L'addition d'un obstacle au bord Ouest du bassin n'a pas beaucoup de conséquences dans la description eulérienne, alors qu'au contraire les propriétés lagrangiennes de l'écoulement sont altérées de manière importante. En effet, dans le cas où l'injection varie au cours du temps, certaines masses d'eau sont déviées du Courant Profond de Bord Ouest vers l'intérieur de l'océan profond au voisinage de l'obstacle. Une fois dans l'intérieur du bassin, ces masses d'eau intègrent l'écoulement vers le Nord. Cette découverte illustre le paradoxe des Grand Banks (Terre-Neuve): les observations eulériennes montrent un Courant Profond de Bord Ouest continu au voisinage du cap Sud des Grand Banks, alors que les bouées lagrangiennes quittent le Courant Profond de Bord Ouest. En effet, au niveau de ce cap, la quasi-totalité des bouées sont éjectées vers l'intérieur du bassin où elles se déplacent vers le Nord,

alors que le Courant Profond de Bord Ouest en lui-même semble suivre un chemin continu le long de la côte nord américaine.

1 Introduction

1.1 Global Ocean Circulation

The global ocean circulation is an important component of the Earth's climate system. First of all, oceans cover more than two-thirds of the surface of the Earth, so that most of the solar radiation is received by the ocean. Due to the high heat capacity of water, the ocean plays a key role in the storage and transport of the solar heat received at the Earth's surface. Indeed, just the top three meters of ocean hold as much heat as the whole atmosphere above. Besides its heat storage ability, the ocean buffers temperature variations in the atmosphere by redistributing heat around the globe. For instance, the Gulf Stream, a wind-driven major Atlantic current, carries warm water masses from low to high latitudes in the northern hemisphere. Going northward, Gulf Stream water releases heat to the atmosphere, making Northwestern Europe warmer than it otherwise would be. On the other hand, the ocean exchanges gases such as CO_2 with the atmosphere. Concentration of CO_2 in the ocean system varies over time and influences atmospheric CO_2 concentration, which has an impact on the Earth's climate. At last, the ocean system exchanges fresh water with the atmosphere. Thus, the world ocean is one of the main constituents of the global climate, and its study is necessary for the understanding of the global climate system.

Two kinds of ocean circulations are conceptually distinguished by oceanographers. The *gyre* circulation is observed in all ocean basins, where waters are driven in large systems of horizontal ocean currents. The driving mechanism of the gyre circulation is fairly intuitive; water motions are caused by the shear of the wind at the ocean surface. Wind does not directly affect water below a certain depth, but wind-driven surface currents induce motions in the deep ocean. So, wind forcing at the ocean surface can create deep currents.

The *overturning* — or *thermohaline* — circulation is the large-scale ocean circulation including the global deep circulation. Although the overturning circulation is less intuitive than the gyre one, it was already identified by Count Rumford 200 years ago (Warren 1981). In 1751, the captain Henry Ellis discovered the very low temperatures of deep North Atlantic waters thanks to an ingenious device developed by Stephen Hales. It was a surprising discovery since the ocean was thought to be homogeneous below the atmosphere-affected surface layer. This discovery occurs to be very useful to cool water and wines of sailors during the hot journey across the North Atlantic. In 1800, Count Rumford assumed that these very cold waters could only come from polar regions, and inferred the existence of a deep circulation bringing water from polar regions to the deep Atlantic ocean at low latitudes. Water density is an important aspect of the overturning circulation since the density of a water determines its buoyancy and, thus, its equilibrium depth. The term 'thermohaline' refers to the two parameters that fix the density of a water; its temperature and its salinity.

Fig.1 shows a conceptual picture of the global thermohaline circulation. At the deep water formation sites represented on Fig.1 (yellow ovals), interaction with the atmosphere results in a cooling of water, which means a densification. The densified water sinks until it reaches its neutral density level. Actually, it had been proved that the net downward flux of water at a deep water formation site is negligible, because water sinking is compensated by upwards fluxes (Send and Marshall 1998). Deep water formation sites should not be described as sinking zones, but rather as vigorous vertical mixing zones. As a result of the vertical mixing, the cooling induced by the atmosphere acts on the whole water column,

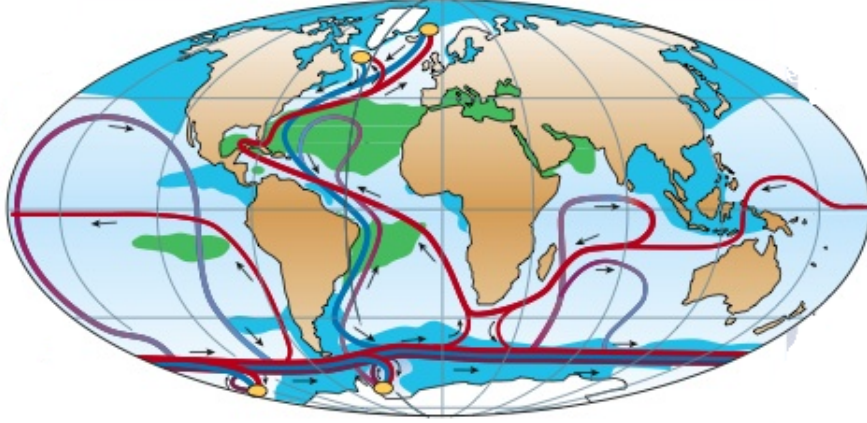


Figure 1: **A simplified conceptual picture of the global thermohaline circulation (Rahmstorf 2002).** Near-surface waters (red lines) flow towards three main deep-water formation regions (yellow ovals) and recirculate at depth (deep currents shown in blue, bottom currents in purple; green shading indicates salinity above 36‰, blue shading indicates salinity below 34‰).

which results in a general densification. The isopycnals (an isopycnal is a surface of constant water density) are displaced upwards; new dense waters are formed. In the North Atlantic ocean, formation of dense water occurs mostly in the Labrador and Norwegian Seas, and the dense water formation rate is estimated to be about 15 Sverdrups (Pedlosky 1998) ($1 \text{ Sverdrup} = 1 \text{ Sv} = 10^6 \text{ m}^3 \text{ s}^{-1}$).

Formation of dense deep water induces movements in the deep ocean. For instance, some dense deep water is transported southward from the Labrador and Norwegian convective sites. This southward transport occurs off the north American coasts, at the western boundary of the North Atlantic. The Deep Western Boundary Current (DWBC) in the North Atlantic is observed thanks to moored current meters which show southward velocities of a few cm s^{-1} to m s^{-1} (Bower and Hunt 2000).

The famous oceanographers Stommel and Arons, applying the theory of Harald Sverdrup (Sverdrup 1947) to an original conceptual framework, were the first to predict the existence of the DWBC in the North Atlantic. The following subsection describes their reasoning.

1.2 The Stommel-Arons Theory

Stommel and Arons were only interested in the deep North Atlantic dynamics. They represent the North Atlantic ocean by a slice of the Earth confined between longitudes ϕ_W, ϕ_E and in the South by the Equator, like on Fig.2. Only the deep ocean, containing dense water, is considered. At the northern corner of the slice, dense water are injected into the deep ocean, with a downwards flux \vec{F}_{in} . This models a dense water formation site.

To respect mass conservation in the deep ocean, some water has to leave the deep ocean thanks to an upwelling whose flux \vec{F}_{out} has the same value as \vec{F}_{in} . Stommel and Arons' main assumption is that the upwelling takes place through the whole surface of the deep ocean. Indeed, no one has ever observed a localized compensating upwelling in the North Atlantic. The absence of observations of a narrow rising region implies that the rising motion is widespread, rendering it too slow to be observed directly.

The upwelling stretches water columns, and water columns responds to their stretching by moving northward. This phenomenon is due to potential vorticity conservation, and will be explained in the subsection 3.4.1. It is counterintuitive, but in the interior of the deep ocean, water moves towards the injection site due to the upwelling.

A southward flowing boundary current is necessary to balance the injection and the northward interior flow. This is easily deduced thanks to the study of mass balance in the part of the deep ocean contained between the North Pole and the latitude θ (see Fig.2). Water enters this ocean portion at the injection site and at the latitude θ (by the northward interior flux). The outgoing flux, through the surface confined between the North Pole and θ , is far too small to compensate the two entering fluxes. Consequently, a boundary southward flux that enables a water output must exist. The Sverdrup theory (Sverdrup 1947) predicts that boundary currents occur only at West of the basins. This is the first prediction of the Deep Western Boundary Current (DWBC) in the North Atlantic. Later, observations of relatively strong southward velocities off the north American coasts confirm this prediction.

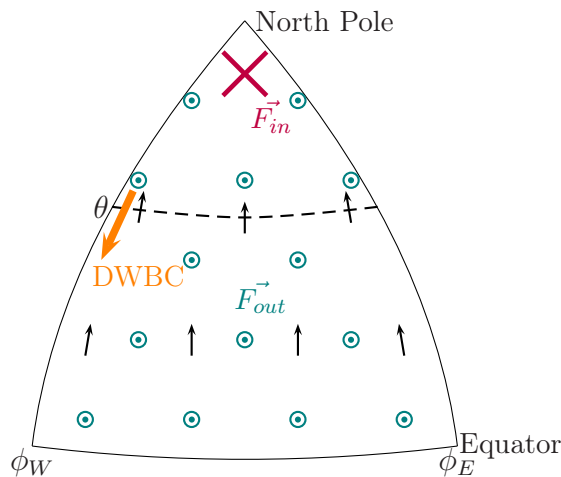


Figure 2: **Stommel-Arons model of the deep North Atlantic ocean, and predicted currents.** The deep North Atlantic is represented by a slice of the Earth. Injection of dense water occurs in a localized zone at the northern corner (\vec{F}_{in} , in purple). On the contrary, the upwelling which compensates the injection is widespread over the whole deep ocean surface (\vec{F}_{out} , in green). The northward transport (black arrows) and the DWBC (orange arrow) are the currents predicted by Stommel and Arons.

1.3 Purpose of the Study

The Atlantic Meridional Overturning Circulation (AMOC) is very important in the climate of the Earth. In the past, shut-down of the dense water formation site in the Labrador Sea has already provoked drastic cooling events such as the Young Dryas event. In 2005, Bryden et al. published a paper showing evidence of a 30 per cent slowing of the AMOC between 1957 and 2004 (Bryden et al. 2005). This paper was the base of ongoing controversies about the possible shutdown of the AMOC in the near future, which awakened concerns about the future climate of Europe. Relationships between the different constituents of the AMOC have to be understood to evaluate the effects of potential changes in some of these constituents on the Earth's climate.

The Stommel-Arons theory is based on a very simple model, but enables to explain a lot of deep ocean phenomena. After the papers of Stommel and Arons, studies of the North Atlantic ocean circulation have evolved towards more and more sophisticated models, with multi-layers oceans, complicated basins topographies and atmospheric forcing. . . Most of these approaches do include time variability of the different types of forcing, but effects of the couple injection/upwelling time-variability are not specifically studied because of the numerous other parameters intervening in the ocean dynamics. The purpose of the present work is to keep the simplicity of the Stommel-Arons model, but include time dependence. Effects of several parameters on the deep ocean circulation are tested in the Stommel-Arons framework.

The first parameter is the numerical viscosity value. Different values of numerical viscosity are tested in order to see the consequences on the general deep circulation.

The system is driven by injection and upwelling. These two forcing types operate on different time-scales. The response of the system to multi time-dependant forcing types is studied here.

Another issue is the pathways of the lower branch of the AMOC in the Grand Banks region. Although the DWBC seems to be continuous along the north American coast according to moored current meters observations, observations using different buoys types failed to show this continuous export path in the Grand Banks region (Fischer and Schott 2002). Lagrangian numerical studies show that a large part of deep water loses its adherence to the DWBC and is diverted into the interior near the southern tip of the Grand Banks (Getzlaff et al. 2006). Mechanisms of this loss of adherence to the DWBC are unknown nowadays. One hypothesis is that the presence of the obstacle creates eddies that are torn apart from the DWBC and then join the northward interior flow. An obstacle will be present in some of the numerical simulations to see if eddies are formed and detached from the DWBC.

In parallel to my numerical simulations, a laboratory experiment imitating the numerical experiment is lead by another LEGI staff. It will be interesting to compare the results of both experiments in future studies.

2 Physical Model based on the Stommel Arons Model

The purpose is to study the characteristic time scales of the deep circulation driven by an injection of water in the deep ocean. The deep North Atlantic limb of the Meridional Overturning Circulation inspires me during the elaboration of my simplified model.

The ocean basin is represented by a square based right prism, with a base of $L_x \cdot L_y = 3,000 \cdot 3,000 \text{ km}^2$ (see Fig.3.B). Both the bottom of the basin and the surface of the ocean are flat (see Fig.3.A).

The water column is divided into two parts: deep waters, with a density ρ_b , and surface waters, with a density ρ_u (see Fig.3.A). In the ocean, calm deep waters are indeed dissociated from the upper layer by the thermocline, a layer where temperature gradients are very steep. In my highly simplified model, the thermocline is represented by a surface separating the dense deep ocean from the less dense surface ocean ($\rho_b > \rho_u$). Each ocean layer is homogeneous. The difference of density between the two layers comes from a temperature difference: the deep ocean is 5 K colder than the surface ocean.

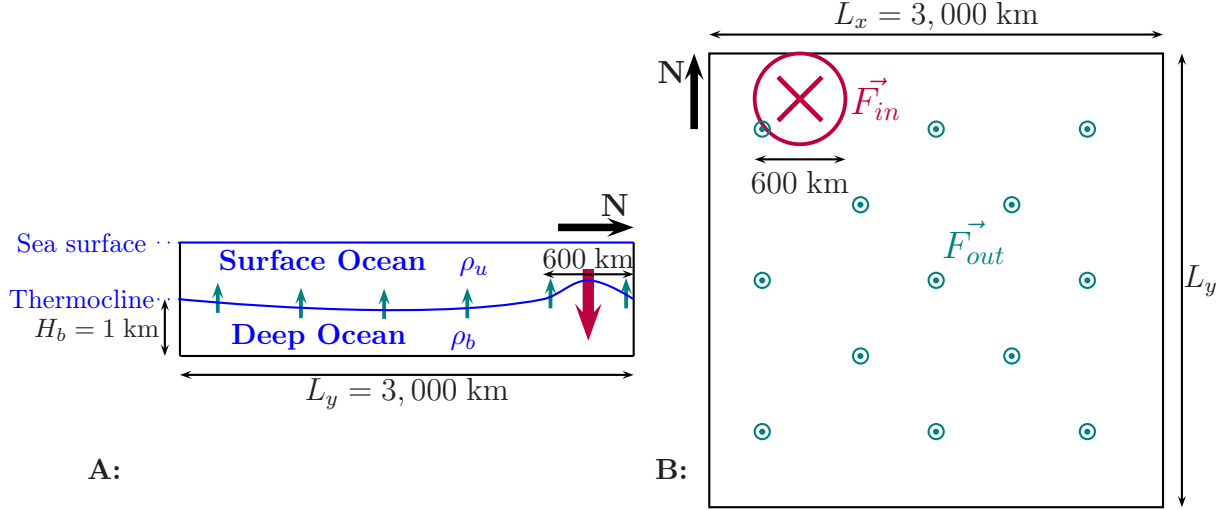


Figure 3: **A: Latitudinal cross-section of the modelled ocean, with a vertical stretching.** The thermocline separates the deep ocean (with a density ρ_b) from the surface ocean (with a density ρ_u). **B: Above-view schema of the deep ocean.** The surface ocean has been slipped off in order to have an above-view of the thermocline surface. Water is injected into the deep ocean at the northwestern corner of the thermocline (pink arrow), in a 600 km diameter zone (pink circle). F_{in} is the flux of water injected into the deep ocean. The small green arrows show that water leaves the deep ocean by an upwelling spread over the whole thermocline. F_{out} is the upwelling flux. To conserve the total mass of water in the deep ocean, $F_{in} = F_{out} = 15 \text{ Sv}$ on average over one year.

The deep ocean is comprised between the basin bottom and the thermocline. Its initial height is $H_b = 1 \text{ km}$. H_b is negligible in comparison to the horizontal extent of the basin: the deep ocean is a shallow homogeneous fluid layer.

The water stock of the deep ocean is renewed. This renewal sets the deep ocean into motion. The deep ocean receives water with a density ρ_b . There is no density difference between the deep ocean and the water injected into it. Thus, flows observed in the deep ocean are not gravity currents. In the experiments, water mass is conserved within the deep ocean: there is as much removed water as injected water. In the North Atlantic Meridional Overturning Circulation, injection of dense water occurs mostly in the Labrador and Norwegian Seas (see Fig.1). On the contrary, removal of water from the deep ocean does not occur at specific places in this part of the ocean circulation. Thus, in my model the injection of dense water within the deep ocean occurs in a zone localized at the northwestern corner of the basin, whereas the removal of water is made by an upwelling through the whole surface of the thermocline, as show in Fig.3. The magnitude of the injection zone diameter is 600 km, as often in the numerical simulations of the AMOC (Spall 2004). The strength of the Atlantic Meridional Overturning Circulation (AMOC) is generally estimated to be about 15 Sv (1 Sv=1 Sverdrup= $10^6 \text{ m}^3 \text{ s}^{-1}$) on average over one year (Hofmann and Rahmstorf 2009). This is the value used for the fluxes of water injected into and removed from the deep ocean. Contrary to the Stommel Arons model, the present model includes time variability of both the injection and the upwelling. Fluxes of injection and upwelling can either be constant or time-dependant. Over one year, their average is equal to 15 Sv .

My model takes into account the influence of the rotation of the Earth on ocean flows. The rotation vector of the Earth, called $\vec{\Omega}$, points northward along the South-North axis, and has a magnitude of $\Omega = 2\pi/T = 7.3 \cdot 10^{-5} \text{ s}^{-1}$ where $T = 24 \cdot 60 \cdot 60 \text{ s}$ is the Earth's rotation period. At each point of the surface of the Earth, $\vec{\Omega}$ can be described by a vertical

and a tangential components. For large scale oceanic motion, the horizontal component of the rotation vector $\vec{\Omega}$ is usually neglected; this is called the *traditional approximation*. Thus, at a latitude θ , only the vertical component of the rotation vector is considered, with a value of $\Omega \cdot \sin \theta$. Twice the vertical component of the rotation vector is denoted by $f = 2\Omega \cdot \sin \theta$ and called Coriolis parameter. In my model, the *beta-plane approximation* is used; instead of being a sinusoidal function of the latitude, f is approximated by a linear function which increases going northward. β is the latitudinal derivative of the Coriolis parameter f in the geometry beta-plane.

The dynamics of age tracers, for instance radioactive tracers such as ^{14}C , can also be simulated. They will give information on the age of specific water masses. The age tracers will help to visualize structures of the deep ocean circulation.

3 Mathematical Model based on the Shallow Water Equations

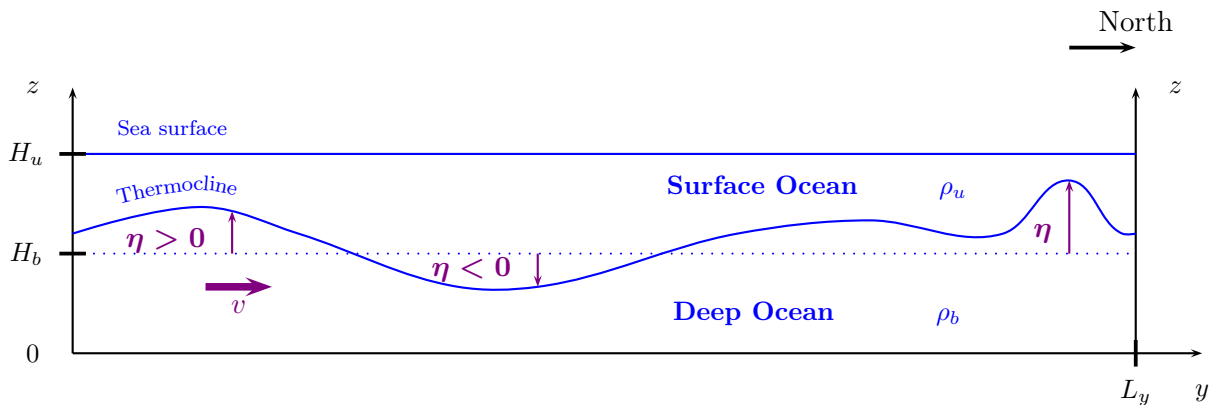


Figure 4: **Latitudinal cross-section of the modelled ocean, with a vertical stretching.** The basin, whose total height is H_u , is divided into the surface ocean (with a density ρ_u) and the deep ocean (with a density ρ_b) by the thermocline. The present study concerns only the deep ocean comprised between the bottom basin and the thermocline. Initially, the thermocline is flat and at the constant height $H_b=1$ km. Over time t , the thermocline topography η (thin purple arrows) changes and becomes space dependent. The height of the thermocline is $H_b + \eta(x, y, t)$. v , the meridional component of the velocity (thick purple arrow), is positive going northward. The zonal component of the velocity u is positive going eastward (not represented here).

The basin is described in a 3D cartesian frame, where x represents the longitude, y the latitude, and z the vertical axis. Fig.4 shows a section of the modelled ocean along latitude.

From now, I am only interested in the dynamics of the dense deep ocean. The dynamics of the surface ocean is totally ignored, it has absolutely no influence over the dynamics of the deep ocean in my model.

The deep ocean is not stratified; the density ρ_b is homogenous within it. The circulation of the deep ocean is only driven by injection or loss of dense water. The density of the water injected into the deep ocean is ρ_b .

The deep ocean's height is negligible compared with its horizontal extent. Indeed, the initial deep ocean's height is $H_b = 1$ km, whereas $L_x = L_y = 3,000$ km. Thus, the deep

ocean can be seen as a shallow homogenous layer of fluid. It is why the *Shallow Water model* is chosen to study the deep ocean dynamics.

The thermocline is the top of the deep ocean. The shape of the thermocline varies in time and space. Every moment t , η (m) is the difference between the initial height of the thermocline H_b and the current one (see Fig.4), that is to say the topography of the thermocline. η depends on space and time. The thermocline height is $H_b + \eta(x, y, t)$.

3.1 Shallow Water Equations derived from the Navier-Stokes Equations

The Shallow Water equations derive from the Navier-Stokes equations, which describe the conservation of momentum for an incompressible fluid. For a fluid particle belonging to the deep ocean, the Navier-Stokes equations are:

$$\left\{ \begin{array}{l} \partial_t \vec{u} + (\vec{u} \cdot \vec{\nabla}) \vec{u} = -\frac{1}{\rho_b} \vec{\nabla} P + \vec{g} + \nu \nabla^2 \vec{u} \\ \partial_x u + \partial_y v + \partial_z w = 0 \end{array} \right. \quad (1)$$

where \vec{u} is the velocity vector (m s^{-1}), with u , v and w respectively its zonal, meridional and vertical component. P is the pressure (Pa), \vec{g} the acceleration of gravity vector (m s^{-2}), ρ_b the density (kg m^{-3}) and ν the cinematic viscosity ($\text{m}^2 \text{s}^{-1}$) of deep waters. In the Shallow Water framework, some simplifications are applied to the equation system (1) in order to enable its resolution:

- w is negligible in comparison to u and v . Indeed, as $H_b \ll L_x, L_y$, the incompressibility equation implies that $w \ll u, v$
- the value of the vertical velocity w is very small. If w is assumed to be ≈ 0 , the projection of the Navier-Stokes equation along z is approximated by the *hydrostatic equation* $\partial_z P = -\rho g$. This means that the pressure P does not depend on the velocity of the fluid, but only on the depth of fluid particles
- the bottom friction is neglected in the Shallow Water model. With this assumption, it can be shown that u and v do not depend on the vertical direction: $\partial_z u = \partial_z v = 0$. Therefore, the horizontal velocity is constant along each water column. This independency is worth notice for the further visualization of our results; although the deep ocean is thought as a volume, the vertical axis is not very important because the horizontal velocity does not change along it. Thus, concerning the horizontal velocity, our deep ocean can be seen as a surface since the depth does not bring any more information.

The pressure is considered to be hydrostatic in the Shallow Water model (cf second item). At a given depth z of the deep ocean, the pressure is generated by the weigh of the above water column (see Fig.4):

$$\begin{aligned} P(x, y, z, t) &= \rho_b g (H_b + \eta(x, y, t) - z) + \rho_u g (H_u - H_b - \eta(x, y, t)) \\ \Rightarrow \left\{ \begin{array}{l} \partial_x P = (\rho_b - \rho_u) g \partial_x \eta \\ \partial_y P = (\rho_b - \rho_u) g \partial_y \eta \end{array} \right. \end{aligned}$$

On another hand, the rotation of the Earth has a strong influence on large-scale oceanic circulation. Like it was said in the previous paragraph 2, the basin is considered to rotate

around an upwards vertical axis of magnitude $f/2$ (it is the traditional approximation). To take into account this rotation, one must add a term accounting for the Coriolis pseudo-force to the time derivative of the velocity. The components of this Coriolis term along x and y are respectively $-fv$ and fu .

All of this leads to two of the Shallow-Water equations:

$$\begin{cases} \partial_t u - fv + u\partial_x u + v\partial_y u + \frac{\rho_b - \rho_u}{\rho_b} g \partial_x \eta = \nu(\partial_{xx}^2 + \partial_{yy}^2)u \\ \partial_t v + fu + u\partial_x v + v\partial_y v + \frac{\rho_b - \rho_u}{\rho_b} g \partial_y \eta = \nu(\partial_{xx}^2 + \partial_{yy}^2)v \end{cases}$$

In the beta-plane geometry, f varies linearly with the latitude: $f = f_0 + \beta y$, with $y = [0, L_y]$. $f_0 = 2\Omega \sin \theta_0$ and $\beta = 2(\Omega/R) \cos \theta_0$, with R the Earth radius, are both constant. In my simulations f_0 and θ_0 are calculated for the Newfoundland's latitude: 50° . The difference between ρ_b and ρ_u is due to a temperature difference of 5 K. The term $\frac{\rho_b - \rho_u}{\rho_b}$ can be calculated thanks to the Boussinesq equation $\rho_b = \rho_u[1 - \alpha(T_b - T_u)]$, with $\alpha \approx 2 \cdot 10^{-4} \text{ K}^{-1}$ the volumetric coefficient of thermal expansion.

3.2 Third Shallow Water Equation derived from the Free-Surface Equation

The thermocline, located at the height $H_b + \eta$, is the interface between two fluid layers: it is a free-surface F , with a free-surface equation:

$$\begin{cases} F(\vec{x}, t) = H_b + \eta(x, y, t) - z = 0 \\ \frac{DF}{Dt} = \frac{\partial F}{\partial t} + \vec{u} \cdot \vec{\nabla} F = 0 \end{cases} \quad \text{with } z \in \text{thermocline} \quad (2)$$

In the Shallow Water model the horizontal velocity is z -independent ($\partial_z u = \partial_z v = 0$), therefore the derivation of the incompressibility equation by z results in $\partial_{zz}^2 w = 0$.

The combination of (2), the incompressibility equation, $\partial_{zz}^2 w = 0$ and the following boundary condition on w leads us to establishing the third Shallow Water equation:

$$\partial_t \eta + \partial_x[(H_b + \eta)u] + \partial_y[(H_b + \eta)v] = 0$$

In conclusion, the Shallow Water equations which describe the dynamics of the deep ocean are:

$$\begin{cases} \partial_t u - fv + u\partial_x u + v\partial_y u + g'\partial_x \eta = \nu(\partial_{xx}^2 + \partial_{yy}^2)u \\ \partial_t v + fu + u\partial_x v + v\partial_y v + g'\partial_y \eta = \nu(\partial_{xx}^2 + \partial_{yy}^2)v \\ \partial_t \eta + \partial_x[(H_b + \eta)u] + \partial_y[(H_b + \eta)v] = 0 \end{cases} \quad \text{with } g' = \frac{\rho_b - \rho_u}{\rho_b} g \quad (3)$$

3.3 Initial and Boundary Conditions

Initially, the deep ocean is at rest. Its thermocline is flat at the height H_b and there is no velocity: $\eta(x, y, 0) = 0$ and $\vec{u}(x, y, 0) = \vec{0}$. Then, the topography of the thermocline changes, initiating water motions in the deep ocean.

Some conditions are applied to the lateral edges of the basin. The first one is the impermeability condition: $u = 0$ on the western and eastern edges; $v = 0$ on the southern and northern edges. The second one is the no-slip condition: $v = 0$ on the western and eastern edges; $u = 0$ on the southern and northern edges. Lastly, the gradients of η across the lateral edges are null in order to prevent the diffusion of η through them: $\partial_x \eta = 0$ on the western and eastern edges; $\partial_y \eta = 0$ on the southern and northern edges.

The impermeability condition is also applied to the bottom of the deep ocean: $w = 0$ at the basin bottom. On another hand, the Shallow Water model implicitly implies the free-slip condition at the basin bottom, since the bottom friction is neglected; and at the thermocline, since it is a free-surface.

3.4 Quantities Conserved by the Non-Linearized Shallow Water Equations

If the viscous term of the Shallow Water model is neglected, the equations are:

$$\begin{cases} \partial_t u - fv + u\partial_x u + v\partial_y u + g'\partial_x \eta = 0 \\ \partial_t v + fu + u\partial_x v + v\partial_y v + g'\partial_y \eta = 0 \\ \partial_t \eta + \partial_x[(H_b + \eta)u] + \partial_y[(H_b + \eta)v] = 0 \end{cases} \quad (4)$$

This paragraph aims at proving that certain quantities are conserved by these equations. The following calculations can easily be found in the literature for the linearized Shallow Water equations. Here, I prove that the results of the linearized case can also be applied to the non-linearized Shallow Water equations.

3.4.1 Potential Vorticity Conservation of Every Water Column

If ∂_y of the (4) first equation is subtracted to ∂_x of the (4) second equation:

$$\begin{aligned} 0 &= \partial_t \partial_x v + f \partial_x u + \partial_x(u \partial_x v) + \partial_x(v \partial_y v) + g' \partial_x \partial_y \eta \\ &\quad - \partial_t \partial_y u + \partial_y(fv) - \partial_y(u \partial_x u) - \partial_y(v \partial_y u) - g' \partial_y \partial_x \eta \\ 0 &= \partial_t \partial_x v + f \partial_x u + \partial_x u \partial_x v + u \partial_{xx}^2 v + \partial_x v \partial_y v + v \partial_x \partial_y v \\ &\quad - \partial_t \partial_y u + f \partial_y v + v \partial_y f - \partial_y u \partial_x u - u \partial_y \partial_x u - \partial_y v \partial_y u - v \partial_{yy}^2 u \\ 0 &= \partial_t (\partial_x v - \partial_y u) + u \partial_x (\partial_x v - \partial_y u) + v \partial_y (\partial_x v - \partial_y u) \\ &\quad (\partial_x u + \partial_y v) (\partial_x v - \partial_y u + f) + v \partial_y f \end{aligned}$$

Since $\partial_t f = \partial_x f = 0$, these terms can be added in the equation :

$$\begin{aligned} 0 &= \partial_t (\partial_x v - \partial_y u) + u \partial_x (\partial_x v - \partial_y u) + v \partial_y (\partial_x v - \partial_y u) \\ &\quad (\partial_x u + \partial_y v) (\partial_x v - \partial_y u + f) + \partial_t f + u \partial_x f + v \partial_y f \end{aligned}$$

$\zeta = \partial_x v - \partial_y u$ is called the *vorticity*. In the simplest sense, vorticity is the tendency to spin of a fluid parcel. One can remember that in the Shallow Water model, u and v are the same along a given water column ($\partial_z u = \partial_z v = 0$). Thus, the vorticity ζ is constant along a given water column. In the Shallow Water framework, the vorticity of a fluid parcel is actually the vorticity of the whole water column it belongs to.

The previous equation equals:

$$\partial_t(\zeta + f) + u \partial_x(\zeta + f) + v \partial_y(\zeta + f) = -(\partial_x u + \partial_y v)(\zeta + f)$$

If one considers a 2D frame with its x and y axis, then the left term of the above equation is the material derivative of $\zeta + f$:

$$\frac{D(\zeta + f)}{Dt} = -(\partial_x u + \partial_y v)(\zeta + f) \quad (5)$$

On the other hand, as H_b is constant in time and space, the third term of (4) is equivalent to:

$$\begin{aligned} 0 &= \partial_t(H_b + \eta) + \partial_x[(H_b + \eta)u] + \partial_y[(H_b + \eta)v] \\ &= \partial_t(H_b + \eta) + u\partial_x(H_b + \eta) + (H_b + \eta)\partial_x u + v\partial_y(H_b + \eta) + (H_b + \eta)\partial_y v \\ &= \partial_t(H_b + \eta) + u\partial_x(H_b + \eta) + v\partial_y(H_b + \eta) + (\partial_x u + \partial_y v)(H_b + \eta) \end{aligned}$$

Here is the material derivative of $H_b + \eta$ in a 2D frame:

$$\frac{D(H_b + \eta)}{Dt} = -(\partial_x u + \partial_y v)(H_b + \eta) \quad (6)$$

Thanks to (5), the horizontal divergence $\partial_x u + \partial_y v$ is expressed in terms of $\zeta + f$, and injected into (6):

$$\frac{D(H_b + \eta)}{Dt} = \frac{H_b + \eta}{\zeta + f} \frac{D(\zeta + f)}{Dt}$$

By multiplying this equation by $\frac{\zeta + f}{(H_b + \eta)^2}$:

$$\begin{aligned} \frac{1}{H_b + \eta} \frac{D(\zeta + f)}{Dt} - \frac{\zeta + f}{(H_b + \eta)^2} \frac{D(H_b + \eta)}{Dt} &= 0 \\ \Leftrightarrow \frac{D}{Dt} \left(\frac{\zeta + f}{H_b + \eta} \right) &= 0 \end{aligned} \quad (7)$$

$(\zeta + f)/(H_b + \eta)$ is called the *potential vorticity* of a given fluid parcel. As the horizontal velocity of water parcels is z -independent in the Shallow Water model, the potential vorticity of a fluid parcel is constant along the whole water column containing the parcel. The potential vorticity of a water column is composed of two parts: $f/(H_b + \eta)$, which does not depend explicitly on the velocity of the water column, is the *planetary potential vorticity*, while $\zeta/(H_b + \eta)$ is the *dynamical* part. The relation (7) means that each water column conserves its potential vorticity over time. The two dimensional flow transports the potential vorticity of each water column of the ocean without modifying it.

The conservation of potential vorticity enables simple explanation for some phenomena observed in the ocean. For instance, if a water column is stretched, $H_b + \eta$ increases. In order to conserve its potential vorticity, the water column can either increase its vorticity ζ , which means to spin quicker, or move northward where the Coriolis parameter f is bigger. In the Stommel Arons model 1.2, planetary potential vorticity of water columns is conserved over time, this is why the stretching caused by the upwelling results in a northward displacement.

3.4.2 Energy Conservation of the Whole Deep Ocean

As H_b , the initial height of the thermocline, does not depend neither on space nor on time, (4) is equivalent to:

$$\begin{cases} \partial_t u - fv + u\partial_x u + v\partial_y u + g'\partial_x h = 0 \\ \partial_t v + fu + u\partial_x v + v\partial_y v + g'\partial_y h = 0 \\ \partial_t h + \partial_x[hu] + \partial_y[hv] = 0 \end{cases} \quad \text{with } h = H_b + \eta \quad (8)$$

The mechanical energy ($J = \text{kg m}^2 \text{s}^{-2}$) of the deep ocean as a whole is the sum of the kinetic E_c and potential E_p energies of the entire deep basin:

$$\begin{cases} E_c = \int_0^{L_x} \int_0^{L_y} \left(\frac{1}{2} \cdot \rho_b h \cdot (u^2 + v^2) \right) dx dy. & w \text{ is close to 0, thus neglected} \\ E_p = \int_0^{L_x} \int_0^{L_y} \left(\rho_b h \cdot g' \cdot \frac{h}{2} \right) dx dy. & \text{the mass center of the deep ocean is at the height } \frac{h}{2} \end{cases}$$

Thus, the time derivative of the mechanical energy is:

$$\begin{aligned} \partial_t(E_c + E_p) &= \partial_t \left(\rho_b \int_0^{L_x} \int_0^{L_y} \left(h \cdot \frac{(u^2 + v^2)}{2} + g' \cdot \frac{h^2}{2} \right) dx dy \right) \\ &= \rho_b \int_0^{L_x} \int_0^{L_y} \partial_t \left(h \cdot \frac{(u^2 + v^2)}{2} + g' \cdot \frac{h^2}{2} \right) dx dy \\ &= \rho_b \int_0^{L_x} \int_0^{L_y} \left(\frac{(u^2 + v^2)}{2} \partial_t h + h(u \partial_t u + v \partial_t v) + g' h \partial_t h \right) dx dy \end{aligned}$$

Thanks to $\partial_t h$, $\partial_t u$ and $\partial_t v$ given by (8):

$$\begin{aligned} \partial_t(E_c + E_p) &= \rho_b \int_0^{L_x} \int_0^{L_y} \left(-\frac{(u^2 + v^2)}{2} (\partial_x[hu] + \partial_y[hv]) \right. \\ &\quad + hu(fv - u \partial_x u - v \partial_y u - g' \partial_x h) + hv(-fu - u \partial_x v - v \partial_y v - g' \partial_y h) \\ &\quad \left. + g' h(-\partial_x[hu] - \partial_y[hv]) \right) dx dy \end{aligned}$$

$$\begin{aligned} \partial_t(E_c + E_p) &= \rho_b \int_0^{L_x} \int_0^{L_y} \left(-\frac{u^2}{2} \partial_x[hu] - \frac{u^2}{2} \partial_y[hv] - \frac{v^2}{2} \partial_x[hu] - \frac{v^2}{2} \partial_y[hv] \right. \\ &\quad - hu^2 \partial_x u - huv \partial_y u - hug' \partial_x h - hvu \partial_x v - hv^2 \partial_y v - hv g' \partial_y h \\ &\quad \left. - g' h \partial_x[hu] - g' h \partial_y[hv] \right) dx dy \end{aligned}$$

$$\begin{aligned} \partial_t(E_c + E_p) &= \rho_b \int_0^{L_x} \int_0^{L_y} \left(-\frac{u^2}{2} \partial_x[hu] - \frac{v^2}{2} \partial_x[hu] - hu^2 \partial_x u - hvu \partial_x v \right. \\ &\quad - \frac{u^2}{2} \partial_y[hv] - \frac{v^2}{2} \partial_y[hv] - huv \partial_y u - hv^2 \partial_y v \\ &\quad \left. - g'(uh \partial_x h + vh \partial_y h + h \partial_x[hu] + h \partial_y[hv]) \right) dx dy \end{aligned}$$

$$\begin{aligned} \partial_t(E_c + E_p) &= \rho_b \int_0^{L_x} \int_0^{L_y} \left(-\frac{u^2}{2} \partial_x[hu] - \frac{v^2}{2} \partial_x[hu] - \frac{hu}{2} \partial_x u^2 - \frac{hu}{2} \partial_x v^2 \right. \\ &\quad - \frac{u^2}{2} \partial_y[hv] - \frac{v^2}{2} \partial_y[hv] - \frac{hv}{2} \partial_y u^2 - \frac{hv}{2} \partial_y v^2 \\ &\quad \left. - g'(\partial_x[h^2 u] + \partial_y[h^2 v]) \right) dx dy \end{aligned}$$

$$\begin{aligned} \partial_t(E_c + E_p) &= \rho_b \int_0^{L_x} \int_0^{L_y} \left(-\frac{1}{2} (\partial_x[hu^3] + \partial_x[huv^2] + \partial_y[hu^2 v] + \partial_y[hv^3]) \right. \\ &\quad \left. - g'(\partial_x[h^2 u] + \partial_y[h^2 v]) \right) dx dy \end{aligned}$$

$$\begin{aligned} \partial_t(E_c + E_p) &= -\frac{\rho_b}{2} \int_0^{L_y} [hu^3 + huv^2]_0^{L_x} dy - \frac{\rho_b}{2} \int_0^{L_x} [hu^2 v + hv^3]_0^{L_y} dx \\ &\quad - \rho_b g' \int_0^{L_y} [h^2 u]_0^{L_x} dy - \rho_b g' \int_0^{L_x} [h^2 v]_0^{L_y} dx \end{aligned} \quad (9)$$

The impermeability condition applied to the lateral edges of the basin ($u(0, y, t) = u(L_x, y, t) = v(x, 0, t) = v(x, L_y, t) = 0$) induces that the right term of (9) is null. Consequently, the Shallow Water equations without the viscous terms conserve the mechanical energy of the whole deep ocean along time.

Be careful; (7) and (9) do not concern the same systems. Each water column conserves its potential vorticity over time while being transported by the flow (7). It is not true for the mechanical energy: the energy of a given water column certainly changes with time. But the energy of the deep ocean in its entirety is constant over time (9).

3.5 Mathematical Model of the Injection and the Upwelling

In my simulations, the deep ocean is initially at rest, with null velocities and a flat thermocline. Then, I modify the shape of the thermocline; its height $H_b + \eta$ is now dependent on space (see Fig.4). Consequently, horizontal gradients of η are created, which corresponds to horizontal pressure gradients. Water particles are pushed away from the high pressure zones: the deep ocean is set in motion. The question is: how do I shape the thermocline so that our model reflects the reality?

At the northwestern corner of the basin, dense water enters the deep ocean with an average flux \vec{F}_{in} of 15 Sv over one year. At the injection spot, there is more dense water than in the rest of the deep ocean. As the water is incompressible, the height of the deep ocean is higher at the injection spot than in the rest of the basin. Therefore, the injection is modeled by a bump in the thermocline. In the third equation of (3), I add the term F_{in}^η (m s^{-1}), which creates a bump in the thermocline: $\partial_t \eta = F_{in}^\eta - \partial_x[(H_b + \eta)u] - \partial_y[(H_b + \eta)v]$. F_{in}^η is a 2D gaussian. The center of the gaussian is situated at the northwestern corner of the basin, and the magnitude of its horizontal extent is 600 km in both directions x and y . I shape F_{in}^η so that the volume under the gaussian equals $15 \cdot 10^6 \text{ m}^3$ on average over one year. Thus, every second, $15 \cdot 10^6 \text{ m}^3$ are injected into the deep ocean on average over one year, which corresponds to \vec{F}_{in} .

The upwelling \vec{F}_{out} , occurring through the whole surface of the thermocline, compensates the injection \vec{F}_{in} (see Fig.3). To model this upwelling, I subtract a term F_{out}^η (m s^{-1}) to the third equation of (3): $\partial_t \eta = F_{in}^\eta - F_{out}^\eta - \partial_x[(H_b + \eta)u] - \partial_y[(H_b + \eta)v]$. F_{out}^η is constant over the whole surface of the deep ocean, and the total volume under it is $15 \cdot 10^6 \text{ m}^3$. Each second, $15 \cdot 10^6 \text{ m}^3$ of water are removed from the deep ocean, which corresponds to \vec{F}_{out} .

Thanks to F_{in}^η and F_{out}^η , every second, the deep ocean receives on average $15 \cdot 10^6 \text{ m}^3$ of water at a localized place and loses as much water through the whole thermocline, over one year.

3.6 Mathematical Model of Age Tracers Dynamics

An age tracer is a passive scalar. It is transported by the water flow but does not influence it; it is not present in the Shallow Water equations (3) ruling the deep ocean dynamics.

Initially, the deep ocean is at rest and age tracers are 0-year-old within the whole basin. Every second, age tracers get older. Once the injection starts, new water enters the deep ocean at the injection site, bringing fresh 0-year-old age tracers. Then, age tracers are transported by deep ocean flows while aging every second.

The equation of age tracers $A(x, y, t)$ (s) is:

$$\partial_t A + u \partial_x A + v \partial_y A = 1 \quad (10)$$

Initially, $A = 0$ s within the whole deep ocean. At the injection site, $A = 0$ s. Likewise for η , the gradients of A across the lateral edges are null to prevent A from diffusing through them: $\partial_x A = 0$ on the western and eastern edges; $\partial_y A = 0$ on the southern and northern edges.

4 Numerical Model

A numerical scheme is constructed for the resolution of the Shallow Water equations (3). These equations describe the dynamics of the deep ocean, they do not concern the

surface ocean. Consequently, there is only one layer in our numerical model: the layer representing the deep ocean.

4.1 2D Horizontal Numerical Frame

Fig.5 shows the conventions chosen for the numerical frame. Although the deep ocean is thought as a 3D layer, the numerical frame has only two dimensions x and y . Indeed, u and v are z -independent, and obviously the height of the thermocline $H_b + \eta$ does not depend on z either. Thus, there is no need to work with the vertical axis. The numerical grid is regular and contains $nx \cdot ny = 1,001 \cdot 1,001$ points. The edges of the basin are located in the middle of grid meshes, so that the more external gridpoints are actually outside the ocean basin.

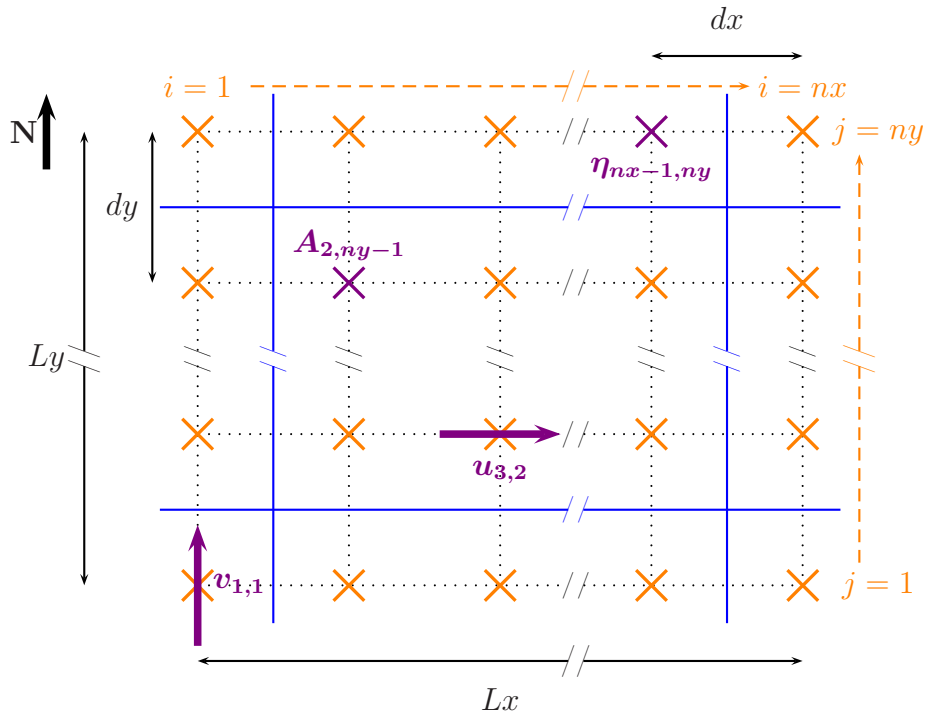


Figure 5: **Above-view of the horizontal numerical frame.** The space is described by a regular grid with $nx \cdot ny = 1,001 \cdot 1,001$ points (orange crosses). Each grid point is characterized by a couple of integers i, j , with $i = [1, nx]$ and $j = [1, ny]$. The grid step is the same in both directions; $dx = dy = L_x/1,000 = 3$ km. The horizontal components of the velocity u, v (purple arrows), the thermocline topography η and age tracers A (purple crosses) are located on the grid points. u is positive going eastwards and v positive going northward. With our conventions, $u_{i,j}$ corresponds to the zonal velocity $u((i-1)dx, (j-1)dy)$. The basin lateral edges are represented by the blue lines. The more external rows of grid points are outside the basin.

4.2 Second-Order Numerical Schemes

All the numerical schemes I use are based on the Taylor series: if a function f has continuous derivatives up to the $(n+1)$ th order, then this function can be expanded in

the following fashion:

$$f(x) = f(x_0) + \frac{f'(x_0)}{1!}(x-x_0) + \frac{f''(x_0)}{2!}(x-x_0)^2 + \dots + \frac{f^{(n)}(x_0)}{n!}(x-x_0)^n + O((x-x_0)^{n+1})$$

My code uses a second-order Runge-Kuta time scheme (Wicker and Skamarock 1998):

$$\begin{cases} f(t + \frac{dt}{2}) = f(t) + \frac{dt}{2}F(t, f(t)) + O(dt^2) \\ f(t + dt) = f(t) + dtF(t + \frac{dt}{2}, f(t + \frac{dt}{2})) + O(dt^2) \end{cases} \quad \text{where } F(t, f(t)) = f'(t)$$

dt is the time step of the experiment. The time derivatives of u, v and η are given in the Shallow Water equations (3), the time derivative of A in the age tracers equation (10). Their space derivatives are expressed at the second order thanks to the centered finite differences method.

4.3 Compelling Conditions for Numerical Stability

One of the principal issue of numerical simulations is the stability. The parameters must be convenient to avoid the 'explosion' of the numerical model. Three points are carefully looked after while elaborating my program:

- the viscous terms of the Shallow Water equations are $\nu(\partial_{xx}^2 u + \partial_{yy}^2 u)$ and $\nu(\partial_{xx}^2 v + \partial_{yy}^2 v)$, where $\nu = 10^{-6} \text{ m}^2 \text{ s}^{-1}$ is the cinematic viscosity of the water. These terms refer to the diffusion of momentum and allow the dissipation of flow energy at the millimeter scale. But in my numerical domain, the smaller scale is the grid step: $dx = 3,000 \text{ m}$, so $10^{-6} \text{ m}^2 \text{ s}^{-1}$ is far too small to enable the dissipation of the energy generated in our simulations. The magnitude chosen for ν is $10^2 - 10^3 \text{ m}^2 \text{ s}^{-1}$. Of course, the smaller value of ν , the better. Unfortunately, it is difficult to forecast whether a numerical model will explode or not. I will try smaller and smaller values of ν until the model explodes.
- likewise the equations for u and v , the third equation of the Shallow Water model requires a diffusive term to prevent the explosion of the numerical model. This term $\kappa(\partial_{xx}^2 \eta + \partial_{yy}^2 \eta)$ is added in the expression of $\partial_t \eta$. The diffusive coefficient $\kappa \text{ (m}^2 \text{ s}^{-1}\text{)}$ is equal to ν . Similarly, a diffusive term $\kappa'(\partial_{xx}^2 A + \partial_{yy}^2 A)$ is added to the time derivative of age tracers given in (10). The third diffusive coefficient is $\kappa' = 100 \text{ m}^2 \text{ s}^{-1}$. Although these diffusive terms are added to stabilize the numerical model, they actually have a physical meaning because molecular diffusion is always present in geophysical phenomena.
- in order to avoid numerical instabilities, the time step dt of the experiments must be inferior to both diffusion and advection characteristic time scales. The diffusion time scale is dx^2/ν . The advective time scale is less immediate. In a non-viscous 1D case, the linearized Shallow Water equations can be reduced to a wave equation, with a wave velocity $\sqrt{g'H_b}$. Thereby, the advective time scale is $dx/\sqrt{g'H_b}$. In conclusion, in my model I must check that $dt < dx^2/\nu$ and $dt < dx/(4\sqrt{g'H_b})$ (this is the Courant-Friedrichs-Lewy condition).

Of course, the numerical model can be improved by decreasing the time and grid steps, allowing the choice of a smaller value for ν and κ . But these modifications drastically increase the calculation duration, and can not be done during a semester internship.

4.4 Numerical Expression of Boundary Conditions thanks to the Centered Finite Differences Method

The impermeability and no-slip conditions at the lateral edges of the basin ($u = v = 0$ at all the lateral edges) are expressed thanks to the centered finite differences method, using the grid points surrounding the edges. For instance, at the western edge, the impermeability condition is (see Fig.5 for notations):

$$u_{\text{W edge}} = u_{1+\frac{1}{2},j} = \frac{u_{1,j} + u_{2,j}}{2} = 0 \Rightarrow u_{1,j} = -u_{2,j}$$

To avoid a diffusion of η and A at the lateral edges of the basin, gradients of η and A are null across the edges. Gradients are expressed with η and A values at the points surrounding the edges, thanks to the centered finite differences method. For instance, at the western edge (see Fig.5 for notations):

$$\begin{aligned} \partial_x \eta_{\text{W edge}} &= \partial_x \eta_{1+\frac{1}{2},j} = \frac{\eta_{2,j} - \eta_{1,j}}{dx} = 0 \Rightarrow \eta_{1,j} = \eta_{2,j} \\ \partial_x A_{\text{W edge}} &= \partial_x A_{1+\frac{1}{2},j} = \frac{A_{2,j} - A_{1,j}}{dx} = 0 \Rightarrow A_{1,j} = A_{2,j} \end{aligned}$$

4.5 Numerical Model of the Injection and Upwelling

Like it was said in 3.5, a forcing term F_{in}^η is added in the expression of $\partial_t \eta$ in order to model the injection. F_{in}^η is a 2D gaussian whose center is located at the point ($x = 600 \text{ km}, y = 2,700 \text{ km}$) (at the northwestern corner of the basin), and whose horizontal extent is about 600 km in both directions. At each second, the volume of water contained under the gaussian enters the deep ocean. Over one year, the average flux of water entering the deep ocean must be about 15 Sv.

The upwelling compensates the injection so that the total water mass is conserved over time within the deep ocean. It means that the average height of the thermocline remains constant and equal to H_b over time: $\langle H_b + \eta \rangle = H_b + \langle \eta \rangle = H_b \Rightarrow \langle \eta \rangle = 0$, where $\langle f \rangle$ is the horizontal space-average of f . On purpose, at each time step, $\langle \eta(x, y, t) \rangle$ is subtracted from $\eta(x, y, t)$ in my numerical model. By that means, the average of $\langle \eta \rangle$ remains 0 and the average height of the thermocline remains H_b over time.

4.6 Implementation of the Numerical Model

The programming language used is Fortran 90. The Fortran program is compiled thanks to the Intel(R) Fortran Compiler, and then the compiled file is executed on one of the LEGI calculators. Results of the experiments are visualized thanks to the free software Scilab and the 2D graph plotting tool Xmgrace.

5 Experiments Parameters

Table.1, in the appendix A, lists the different parameters tested in our numerical experiments. All the experiments were not started simultaneously and their calculations do not last the same time. This is why total durations of the experiments are different. Every simulation is identified by its N° in Table.1. Please refer to this table while reading the following.

The values of $\nu = \kappa$ are comprised between $125 \text{ m}^2 \text{ s}^{-1}$ and $1,000 \text{ m}^2 \text{ s}^{-1}$. For all the values of ν the time step $dt = 200 \text{ s}$, except for $\nu = \kappa = 125 \text{ m}^2 \text{ s}^{-1}$ where $dt = 100 \text{ s}$ to

avoid the explosion of the numerical model. The diffusive coefficient of the age tracers equation is constant; $\kappa' = 100 \text{ m}^2 \text{ s}^{-1}$.

The injection of dense water in the deep ocean is either constant over time or 1-year periodical. In both cases, the deep ocean receives on average about 15 Sv over one year. In the periodical case, the injection follows a gaussian distribution every year. The center of the gaussian is at 6 months, and its deviation is 1 month. It means that in the periodical case, the injection mostly occurs from the 5th to the 7th months of the year, every year.

The deep ocean basin is modeled by a simple square. In half experiments, an obstacle is added: a band of $24,000 \text{ km}^2$ is removed from the basin surface. It is a narrow zonal band coming from the middle of the western edge (see the little schemas in Table.1).

Two different kinds of upwelling are tested. The first kind is the one described in the subsection 4.5: every time step, $\langle \eta(x, y, t) \rangle$ is subtracted from $\eta(x, y, t)$. It means that every time step, the average height of the thermocline is pulled back to its initial height H_b . In this case, the removal of the water is immediate; every time step dt , there is as much removed than injected water. On the other half of the experiments, only $\frac{dt}{1 \text{ year}} \langle \eta(x, y, t) \rangle$ is subtracted from $\eta(x, y, t)$ every time step. In this second case, the water volume injected during dt will take one year before being totally removed from the deep ocean. The deep ocean needs one year to restore its initial volume after an injection of water during dt .

6 Results

One must remember once again that all the following results concern only the circulation in the deep ocean and give no idea about the surface circulation.

6.1 First Approach of the Results with the Simplest Cases: A.1-4 Conditions

My numerical program is first tested for a constant injection and an immediate upwelling in a free-obstacle basin. This enables to establish characteristic features of the deep ocean circulation ruled by the couple injection/upwelling, and to investigate the effect of changes in viscosity ν .

6.1.1 General Structure of the Deep Ocean Circulation

Fig.6 pictures the deep ocean circulation after 20-year simulations for two viscosities $\nu = 1,000$ and $250 \text{ m}^2 \text{ s}^{-1}$. It is the support for the first observations.

The stationary, non-viscous and linearized version of the Shallow Water equations (3) gives the following equation of the geostrophic equilibrium:

$$\begin{cases} fv = g' \partial_x \eta \\ fu = -g' \partial_y \eta \end{cases} \quad \text{with } f > 0 \text{ in the northern hemisphere} \quad (11)$$

Thanks to the geostrophic equilibrium equation (11), it can be proved that bumps in the thermocline turn clockwise in the northern hemisphere. Indeed, the bump representing the injection turns clockwise in the northwestern corner of the basin. Since f increases going northward, $|u|$ is bigger at the southern part of the bump than in the northern

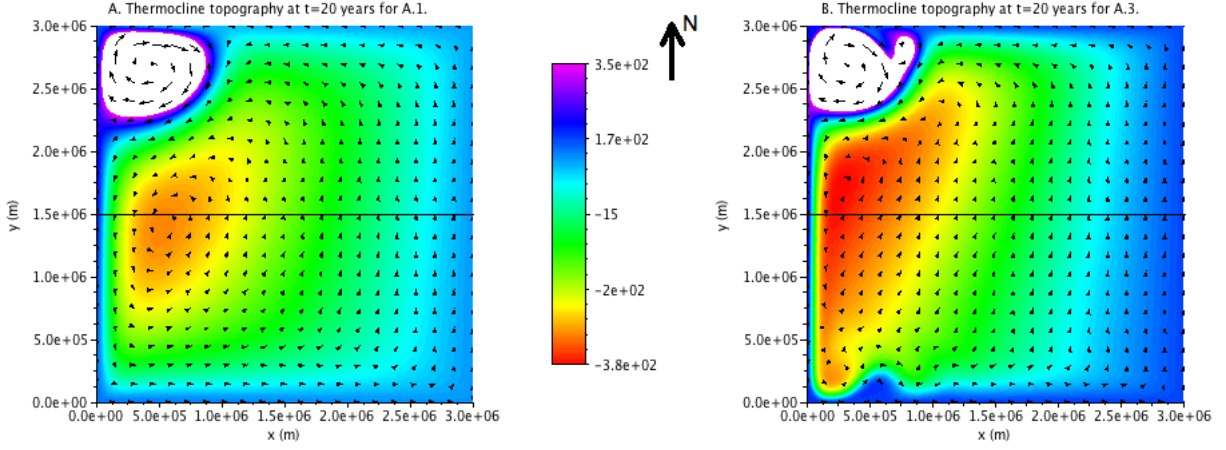


Figure 6: **Above-view of the 20-year-old thermocline for the A.1 (left panel, $\nu = 1,000 \text{ m}^2 \text{ s}^{-1}$) and A.3 (right panel, $\nu = 250 \text{ m}^2 \text{ s}^{-1}$) conditions.** The color bar gives values of the thermocline topography η (m, positive upward). In the non-painted zone, η is higher than 350 m. This big bump in η represents the injection of water in the deep ocean. Little arrows give direction of horizontal velocities (see Fig.7 for values of meridional velocities). Location of the sections shown on Fig.7 is indicated by the black lines in the middle of the basins.

one. As a result of that, the bump is deviated westwards from the injection center ($x = 600 \text{ km}, y = 2,700 \text{ km}$).

The upwelling causes a stretching of water columns. By conservation of potential vorticity ((7), or actually planetary potential vorticity), columns stretching is compensated by a northward displacement, towards bigger values of f . It means that water moves towards the injection site in the interior of the deep ocean. This is fairly counterintuitive, but an interior northward displacement is indeed observed in the major part of the deep ocean. However, conservation of water mass imposes a boundary southward transport. As predicted by the Sverdrup theory, the southward transport takes place at the western boundary. Indeed, at the western boundary of the basin, there is a great elevation of the thermocline height, accompanied by negative meridional velocities v and very low zonal velocities u . Apart from the injection site, the thermocline topography is globally depressed, and the main trend of the deep ocean circulation is counterclockwise. A deep western boundary current settles in all simulations we carried on.

Cross sections of the basin give more accurate information on circulation in the deep ocean. Establishment of deep western boundary currents over time is obvious while looking at successive zonal cross sections Fig.7. Indeed, at the western boundary, gradient of the thermocline topography η becomes steeper, while negative meridional velocities v increase. Mathematically, it means that at the western boundary, $\partial_x \eta$ is negative, likewise v . It is consistent with the geostrophic equilibrium equation (11). When $\partial_x \eta$ becomes more and more negative, so does v .

The thermocline is unsymmetrically depressed; its western rim is higher and steeper than the eastern one. A northward transport, characterized by small positive meridional velocities v , occurs in the major part of the deep ocean.

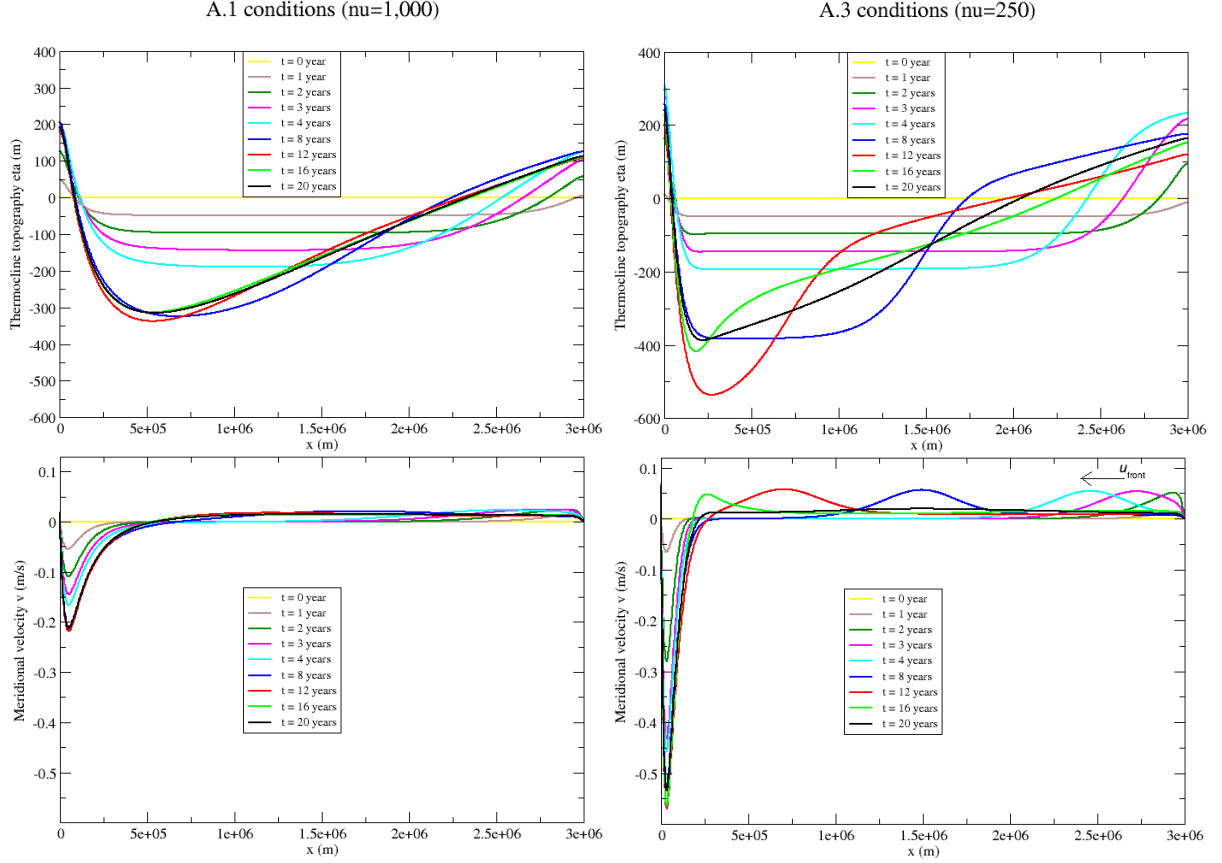


Figure 7: Successive zonal cross sections of the deep ocean for the A.1 (left panel, $\nu = 1,000 \text{ m}^2 \text{ s}^{-1}$) and A.3 (right panel, $\nu = 250 \text{ m}^2 \text{ s}^{-1}$) conditions. See Fig.6 for location of the sections. The upper panel gives η versus x , whereas the lower one gives v versus x . η is positive upward. Negative values of v indicate a southward displacement. The age of each cross section is indicated by the colors. u_{front} is the zonal velocity of the northward flow's front.

6.1.2 The Northward Interior Flow: a general feature

This subsection is dedicated to the study of the northward flow, which is the most extended feature of the deep ocean circulation. Please see Fig.7 for illustrations. At first, the northward flow settles at the eastern boundary of the deep ocean. Between the deep western boundary current and this weak eastern boundary current, meridional velocities v are 0; there is no meridional transport of water in the basin interior during the first years. Over time, the northward flow's front moves towards the interior with a negative zonal velocity u_{front} . The magnitude of u_{front} is 10^{-2} m s^{-1} . Westwards propagation of a front reminds one of the most important kind of atmospheric and oceanographic waves: Rossby waves. Initiation of Rossby waves is due to the variation of the Coriolis parameter f with the latitude. Long-wavelength Rossby waves are non-dispersive waves, whose phase and group velocities are directed westwards and have a magnitude given by $\frac{\beta g' H_b}{f^2} \approx 10^{-2} \text{ m s}^{-1}$ (Gill 1982). Thus, it seems that the establishment of the northward flow is driven by Rossby waves. On Fig.6, the northward flow's front appears to be more advanced in the southern part of the basin. Indeed, the zone of lower η (in red) has a triangular shape with a NE-SW base. On Fig.7, we can see that the bottom of this thermocline depression marks the frontier between the northward and the southward transports (v is positive East and negative West of the depression bottom). This frontier is more western at low latitudes of the basin: the northward flow's front goes faster in

the southern part of the basin. It is consistent with the assumption that Rossby waves rule the northward flow's front settlement, since their velocities decreases going northward because of their denominator f^2 .

In the 20-year-old simulations (black line), the northward flow is well settled for the three A.1, A.2 (data not shown) and A.3 conditions. The magnitude of its meridional velocity v is 10^{-2} m s^{-1} . As it was said before, the northward flow is thought to be due to the upwelling, since the upwelling causes a stretching of water columns responsible of a northward displacement. The relation between the upwelling and the northward flow can be found thanks to the geostrophic equilibrium equations (11). If ∂_x (second equation of (11)) and ∂_y (first equation of (11)) are added:

$$\begin{aligned} f\partial_x u + f\partial_y v + \beta v &= 0 \Rightarrow \beta v = -f(\partial_x u + \partial_y v) \\ \beta v &= f\partial_z w \quad (\text{cf the incompressibility equation}) \end{aligned}$$

What is the magnitude of $\partial_z w \cong \frac{w}{H_b}$? The upwelling removes 15 Sv of water through the whole surface of the thermocline, so:

$$w \cdot L_x L_y = 15 \text{ Sv} \Rightarrow w = \frac{15 \cdot 10^6 \text{ m}^3 \text{ s}^{-1}}{(3 \cdot 10^6)^2 \text{ m}^2} \approx 2 \cdot 10^{-6} \text{ m s}^{-1}$$

Thereby:

$$v = \frac{fw}{\beta H_b} \approx \frac{1.1 \cdot 10^{-4} \text{ s}^{-1} \cdot 2 \cdot 10^{-6} \text{ m s}^{-1}}{1.5 \cdot 10^{-11} \text{ m}^{-1} \text{ s}^{-1} \cdot 1000 \text{ m}} \approx 1 \cdot 10^{-2} \text{ m s}^{-1} \quad (12)$$

The magnitude of the meridional velocity v in the northward transport seems to be related to the upwelling. The viscosity does not intervene in the calculation of v magnitude. 20-years-old results show that when the northward transport is well established in the deep ocean, v does not depend on the viscosity value, since it is the same in the cases A.1 ($\nu = 1,000 \text{ m}^2 \text{ s}^{-1}$), A.2 ($\nu = 500 \text{ m}^2 \text{ s}^{-1}$) and A.3 ($\nu = 250 \text{ m}^2 \text{ s}^{-1}$).

Besides, on the 20-year-old cross sections of the Fig.7 upper panel, one can notice the parallelism of the A.1 and A.3 thermocline slopes everywhere in the basin but at the western boundary. In the zone of the northward interior flow, the slope of the thermocline is $\partial_x \eta \approx 0.17 \text{ m km}^{-1}$ in both cases. It appears that the geostrophic equilibrium is reached in the 20-year-old simulations, because the magnitude of the observed v in the northward interior flow is the same as the magnitude calculated thanks to the first equation of (11), with $\partial_x \eta \approx 0.17 \text{ m km}^{-1}$.

6.1.3 On the Importance of the Numerical Viscosity Value ν in this Simple Model

During the experiment, injection of water brings potential energy to the deep ocean. The system converts this potential energy into kinetic energy. Due to hydrodynamical phenomena, energy is then transferred in an energy cascade from large to small scales. Down the energy cascade, energy is dissipated by viscous and diffusive forces at small scales. Because of the 3 km space resolution of the simulations, the value of the water cinematic viscosity ($10^{-6} \text{ m}^2 \text{ s}^{-1}$) is not sufficient to enable the dissipation of the energy created during the numerical experiment. It is why the numerical values of ν are much higher. Of course, the smaller $\nu = \kappa$ in the numerical model, the more realistic the experiment is. However, it is interesting to compare the results obtained for different ν values. Indeed, I have experienced that it is necessary to diminish the time step dt for avoiding the explosion of the A.4 simulation ($\nu = 125 \text{ m}^2 \text{ s}^{-1}$). But a smaller time step

means a longer calculation process. Consequently, if the results of A.1-4 are not very different, there is no point in reducing again the ν value at the 3 km resolution, because simulations would take too much time for a negligible information gain. In addition, bifurcations could occur between the simulations with different values of ν . A bifurcation is induced by a smooth change in the parameters and causes, after a certain amount of time, a sudden 'qualitative' change in systems' behaviors.

Dependence on the numerical viscosity value ν is very striking in the Deep Western Boundary Current. First of all, meridional velocities v in the DWBC are very different in the simulations A.1-4. The lower panel of Fig.7 well illustrates these differences: the smaller the ν value, the higher the velocities in the DWBC are. In the 20-year-old sections, the maximum negative velocity in the DWBC is -0.21 m s^{-1} in the A.1 conditions and -0.54 m s^{-1} in the A.3 conditions. Second of all, the smaller the ν value, the narrower the zone of southward displacement is. For instance, in the 20-year-old cross sections, the boundary between southward ($v < 0$) and northward ($v > 0$) displacements is located at $x \approx 550 \text{ km}$ in the A.1 conditions, whereas this boundary is located at $x \approx 230 \text{ km}$ in the A.3 conditions. At last, the smaller the ν value, the steeper the gradients of η are at the western boundary. In the A.1 conditions, $\partial_x \eta \approx -2 \text{ m km}^{-1}$ while $\partial_x \eta \approx -4.8 \text{ m km}^{-1}$ in the A.3 conditions.

The viscosity-dependence of the thickness of the deep western boundary layer was first studied by Munk in a linear case (Munk 1950). He described a boundary-layer with a δ_M thickness, where:

$$\delta_M = \sqrt[3]{\frac{\nu}{\beta}}$$

With the ν values tested in the numerical experiments, δ_M is comprised between 20 km (for $\nu = 125 \text{ m}^2 \text{ s}^{-1}$) and 40 km (for $\nu = 1,000 \text{ m}^2 \text{ s}^{-1}$). In the DWBC of the A.1 and A.4 cases, the negative meridional velocity v reaches its maximum value at $dx \approx \delta_M$. So, despite the non-linearity of my model, the decrease of the DWBC thickness with the decrease of ν is well described by the thickness of the Munk layer.

To finish with the influence of the numerical viscosity value, deep circulation at the southern boundaries of the Fig.6 above-views can be observed. The DWBC seems to be laminar with the A.1 conditions (left panel), whereas a 150 km diameter anticyclonic (=clockwise) eddy is formed at the southern edge of the basin in the A.3 case (right panel). The Reynolds number in the DWBC is $Re = \frac{v_{DWBC} \delta_M}{\nu}$. Calculations show that Re increases from the A.1 to the A.4 conditions, rendering the flow of the DWBC more turbulent and enabling eddies formation.

6.2 Time-Variability of Injection and Upwelling: Differential Effects on the Northward Interior Flow and the DWBC

It has been proved that the formation of dense water is an intermittent process. For instance, in the Labrador Sea, the vigorous convection resulting of the surface water cooling occurs only 3 weeks a year, in winter. Thus, the subsequent dense water formation can not be constant over time. It is why time-variability of the injection is introduced in the present study.

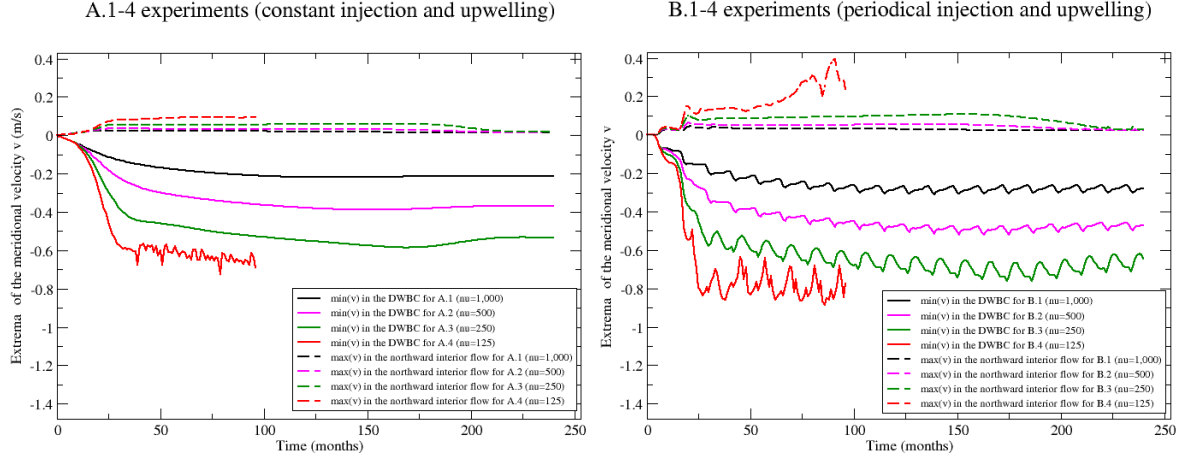


Figure 8: **Time series of the meridional velocity v extrema in the A.1-4 experiments (left panel) and the B.1-4 experiments (right panel), at the zonal cross section localized on Fig.6.** Every month, extrema of the meridional velocity along the zonal cross section are reported here. The v minima (solid lines) are the most negative meridional velocities observed in the DWBC. The v maxima (dashed lines) are the highest meridional velocities observed in the northward interior flow. Line colors indicate the value of the numerical viscosity ν . I haven't got enough time to perform A.4 and B.4 simulations longer than 8 years. All the values of the B.1-4 results are lightly higher than the ones of the A.1-4 results. It just because the amount of water injected was a little bigger in the B.1-4 simulations.

In the experiments B.1-4, the injection is 1 year periodical. Over one year, the forcing applied by the injection is described by a time gaussian with the equation:

$$\exp\left(-\frac{1}{2}\left(\frac{t - 6 \text{ months}}{1 \text{ month}}\right)^2\right) \cdot F_{in}^{\eta}$$

with t in months. F_{in}^{η} notation is defined in the 3.5 subsection.

This time gaussian forcing signifies that the main injection occurs from the 5th month to the 7th month of a year, with a maximal injection in the 6th month. Before the 4th month and after the 8th month, the injection is negligible. This gaussian forcing is applied every year.

As the removal of water is immediate in the A.1-4 and B.1-4 experiments, the upwelling is also 1 year periodical, and is described by the same time gaussian as the injection over one year.

Fig.8 is a way to study the effect of the time-variability of both injection and upwelling on settlement of the DWBC (solid lines) and the northward interior flow (dashed lines). In the left panel experiments, the injection and the upwelling are constant, whereas they are both 1-year periodical in the right panel experiments. General trends of graphs are the same in both panels: velocities in the DWBC and in the northward interior flow increase in the 30 first months, then they stabilize around a given value, with more or less oscillations. At 220 months, velocities of the northward interior flow reach the same value in all simulations. The decrease in the numerical viscosity ν (ν values are indicated by colors) causes stronger velocities everywhere.

In the B.1-4 experiments (with time-varying injection and upwelling), velocities of the DWBC present oscillations with a 1 year period. On the contrary, after 24 months — that is to say after 2 injection pulses; one around the 6th month and one around the 18th — the time evolution of the northward interior flow is almost the same as when the injection and the upwelling are constant; the northward interior flow does not present periodical

oscillations throughout the duration of the simulations.

The experiments B.1-4 have shown that the DWBC and the northward interior flow do not behave the same way when the deep ocean is submitted to a 1 year periodical injection/upwelling couple. If 1 year periodical oscillations do exist in the DWBC, the interior northward current does not show any periodical variations. This is consistent with the fact that the establishment of the northward interior flow is controlled by long-wavelength Rossby waves (cf subsection 6.1.2). Indeed, long-wavelength Rossby waves are slow, so dynamics controlled by them have necessary a long characteristic time-scale, and they can not respond to forcings with a time period smaller than their characteristic time-scale. Consequently, the absence of oscillations in the northward interior flow implies that its dynamics has a characteristic time-scale longer than 1 year.

6.3 Forcing Governing the DWBC Dynamics: Injection or Upwelling?

The upwelling compensating the injection is thought to take place through the whole deep ocean surface, with vertical velocities w too weak to be measured. Because of the absence of observation, dynamics of the upwelling is unknown. In the A, B, C and D simulations, the removal of water occurs simultaneously to the injection; mass conservation is respected at each time step. Thus, the upwelling is either constant or 1 year periodical, according to the type of the injection. But one can make the hypothesis that there is a gap between the injection and the removal of the injected water. The gap is a mass conservation restoring time; the deep ocean takes this restoring time to get rid of a punctual injection of water. The hypothesis of the restoring time between the injection and the upwelling is very probable in the ocean dynamics, because of the inertia of the ocean system.

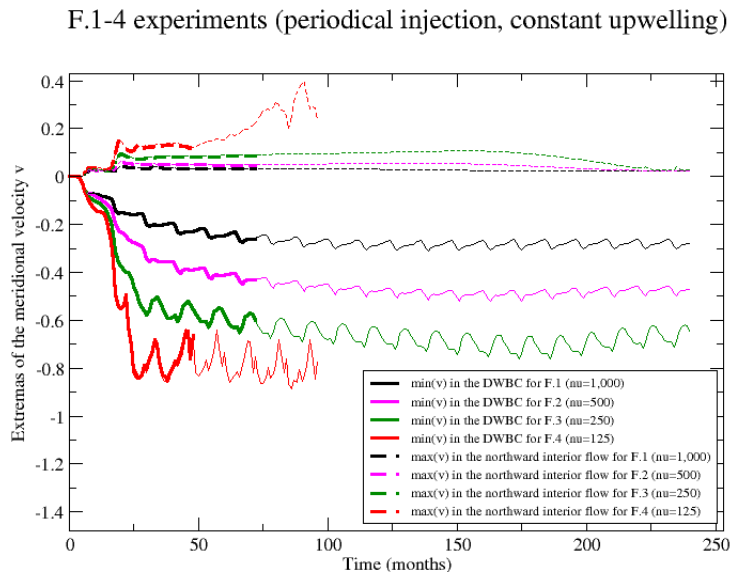


Figure 9: Time series of the meridional velocity v extrema in the F.1-4 experiments (thick lines) superimposed on the B.1-4 experiments (thin lines), at the zonal cross section localized on Fig.6. See Fig.8 for comments.

In the experiments with a restoring time equal to 1 year (E, F, G and H experiments), a given water volume injected into the deep ocean takes 1 year before being completely

removed. Every time step, a very small fraction ($\frac{dt}{1 \text{ year}}$) of this volume is removed from the deep ocean, during 1 year. Mass conservation is verified but on 1 year time scales, not immediately. This time restoring smoothes the possible time variations of the upwelling. Thus, even when the injection is 1 year periodical, the upwelling is almost constant over time.

I run out of time for these simulations, so the oldest experiments are only 6 years old with the 1 year time restoring. The results for the F.1-4 conditions are presented on Fig.9.

In the DWBC and the northward interior flow, extrema of meridional velocities v with the F.1-4 conditions are the same as the ones with the B.1-4 conditions. 1 year periodical oscillations are present in the DWBC, whereas no oscillations are shown in the northward interior flow.

Between the B.1-4 and the F.1-4 conditions, the time restoring is the only different parameter. However, results are the same. This demonstrates that the DWBC dynamics is controlled by the injection. Indeed, in the F.1-4 conditions, the only time-varying forcing is the injection, and the DWBC shows time-variations with the same time period than the injection.

Once again, the northward interior flow does not react to the 1 year periodical time-variations of the injection, proving that its dynamics is not controlled by the injection characteristic time-scales. In addition, the northward interior flow is the same with a constant upwelling as with a 1 year periodical upwelling. Although the northward velocity seems to be directly related to the upwelling in the equation (12), its dynamics time-scales are not dominated by the upwelling characteristic time-scales tested in the present simulations. The characteristic time-scales of the northward interior flow's dynamics are longer than 1 year.

6.4 Obstacle and Periodical Injection: an Interesting Couple...

In the C, D, G and H simulations, a simple obstacle has been added at the western boundary of the basin. The purpose is to study the behavior of the DWBC in the vicinity of the obstacle. This obstacle models continental obstacles like the southern tip of the Grand Banks (Newfoundlands), where the pathways of water parcels belonging to the DWBC seems to be complicated (Fischer and Schott 2002).

When the injection is constant, the addition of the obstacle does not change the deep ocean general circulation. The DWBC simply follows the obstacle without consequences on the rest of the circulation.

An interesting observation is made in the D.3 simulation (with a 1 year periodical injection), thanks to age tracers. Successive above-view of the deep ocean are presented Fig.10 for the D.3 simulation.

The left panel of Fig.10 (appendix B), compared with the right panel of Fig.6, shows that the obstacle does not perturb a lot the general circulation in the deep ocean. The DWBC follows the obstacle, but the rest of the circulation is not very different than the one in Fig.6.

Initially, age tracers A are 0-year-old everywhere in the deep ocean. Every month, these age tracers get 1 month older (they age with the deep ocean). The new water entering at the injection site carries fresh 0-year-old age tracers. Once they are in the deep ocean, the fresh age tracers age too. All the age tracers are passively transported by the deep ocean flows. In the 150-month-old simulation of the Fig.10 right panel, injection is visualized by the 600 km diameter spot of 0-year-old age tracers, in the northwestern

corner of the basin. Over time, this spot dwindles since the injection decreases until the next year. Once they are in the basin, age tracers are transported by the DWBC until the southwestern corner. Then, they are transported eastwards along the southern boundary, overshooting the eddy. East of the eddy, age tracers penetrate into the northward interior flow. As the northward interior flow is not yet completely established, meridional velocities v are higher in its western part (see the meridional velocities during the propagation of the northward interior flow's front, Fig.7 lower right plot). Thus, age tracers move northward faster in the western part of the northward interior flow than in the eastern one. This explains the lineation structure in the interior of the basin (blue lineations correspond to former injection pulses, in previous years).

But the most surprising phenomena in the time-evolution of age tracers is what happens in the vicinity of the obstacle. Between $t=153$ and 156 months, a strip of young water (about 38-year-old in the center of the strip) is progressively detached from the DWBC (indicated by black arrows in Fig.10 right panel). At $t=159$ months, this young strip of water is totally separated from the DWBC. It has been deviated from the DWBC to the interior of the basin, where it is carried northward by the northward interior flow.

7 Discussion of the Results

The space resolution of the present simulations (3 km) is fine compared with the one of the climatic models (200 km), enabling the visualization of smaller scale structures, such as the 150 km diameter eddy cited in the previous subsection. In Fig.8 left panel, the meridional velocities v of the A.4 simulation ($\nu = 125 \text{ m}^2 \text{ s}^{-1}$) present small-magnitude time oscillations in the DWBC, whereas the injection and the upwelling are constant. These oscillations could be due to the presence of small-scale eddies in the turbulent DWBC, or to numerical instabilities. However, numerical instabilities are less probable because of the small magnitude of the oscillations. The simulation has to be continued to see if these oscillations provoke the explosion of the numerical model. Despite the simplicity of the model, changes in the numerical viscosity value ν provoke well visible differences in the deep circulation. This encourages the use of this simple model with finer time and scale resolutions in order to discover other structures, with smaller scales.

Time-variability of the injection and the upwelling enables to distinguish the rapid dynamics of the DWBC from the slow dynamics of the northward interior flow. The DWBC dynamics is dominated by the injection time-scales. However, relationships between the DWBC and the time-varying injection need further investigation. The response of the DWBC to the time-variations of the injection is not immediate, there is a latency. For instance, after an injection pulse in the middle of a year, the injection is totally stopped during few months. The DWBC starts to decrease, but it does not have time to vanish in one year, before a new injection. Thus, other time-scales intervene in the DWBC, for instance the advective time-scale. The northward interior flow's time-scales seem to be dominated by the time-scales of the long-wavelength Rossby waves. The northward interior flow does not respond to 1 year period variability in the injection/upwelling couple. This fact is surprising because in the equation (12), the meridional velocity of the northward interior flow is directly related to the upwelling.

The mathematical model proposed here has an Eulerian point of view. In this Eulerian point of view, the presence of an obstacle does not have a strong impact of the flow properties. The age tracers, on the contrary, follow the flow with a Lagrangian point of view. Properties of flow described by the age tracers point of view are considerably

affected by the presence of an obstacle when the injection is time-dependent and the numerical stability small enough. Indeed, age tracer masses are diverted from the DWBC to the interior of the basin, where they are caught by the northward interior flow in the D.3 simulation. This result is in agreement with the conclusions of (Getzlaff et al. 2006) and the observations of (Fischer and Schott 2002). One hypothesis to explain the division of the DWBC was that the presence of the obstacle caused turbulent eddies that could overshoot the obstacle, carrying age tracers masses away from the DWBC. But the present results invalidate this hypothesis since none eddies are observed in the vicinity of the obstacle.

8 Conclusions and Perspectives

This study rejuvenates the Stommel Arons model by integrating time-variability in the forcing couple injection/upwelling. The opposition between the rapid DWBC dynamics and the slow northward interior flow dynamics is quantified. In the future, quantitative studies have to be made to precisely establish the time-scales intervening in the two dynamics, and to better understand the interaction of the dynamics at two different time-scales.

Integration of age tracers in the model enables to confirm a 'paradox' between the Lagrangian and the Eulerian point of views. Age tracers can be, in addition, used to establish the residence time of water masses in the deep ocean. Experiments of several hundred of years of dynamics are necessary. Such calculations take several months on present computers, exceeding the characteristic time-scale of a M2R internship!

References

- Bower, A. S. and Hunt, H. D.: 2000, Lagrangian Observations of the Deep Western Boundary Current in the North Atlantic Ocean. Part I: Large-Scale Pathways and Spreading Rates, *J. Phys. Oceanogr.* **30**, 764–783.
- Bryden, H. L., Longworth, H. R. and Cunningham, S. A.: 2005, Slowing of the Atlantic meridional overturning circulation at 25°N, *Nature* **438**, 655–657.
- Fischer, J. and Schott, F. A.: 2002, Labrador Sea Water tracked by profiling floats-From the Boundary current into the open North Atlantic, *J. Phys. Oceanogr.* **32**, 573–584.
- Getzlaff, K., Boning, C. W. and Dengg, J.: 2006, Labrador Sea Water tracked by profiling floats-From the Boundary current into the open North Atlantic, *Geophys. Res. Lett.* **33**, L21S08.
- Gill, A. E.: 1982, *Atmosphere-Ocean Dynamics*, Academic Press.
- Hofmann, M. and Rahmstorf, S.: 2009, On the stability of the Atlantic meridional overturning circulation, *Proc. Natl. Acad. Sci.* **106**, 20584–20589.
- Munk, W. H.: 1950, On the Wind-Driven Ocean Circulation, *J. Meteorol.* **7**, 79–93.
- Pedlosky, J.: 1998, *Ocean Circulation Theory*, Springer.
- Rahmstorf, S.: 2002, Ocean circulation and climate during the past 120,000 years, *Nature* **419**, 207–214.

- Send, U. and Marshall, J.: 1998, Integral Effects of Deep convection, *J. Phys. Oceanogr.* **25**, 855–872.
- Spall, M. A.: 2004, Boundary Currents and Watermass Transformation in Marginal Seas, *J. Phys. Oceanogr.* **34**, 1197–1213.
- Sverdrup, H. U.: 1947, Wind-driven currents in a baroclinic ocean, with application to the equatorial currents of the eastern Pacific, *Proc. Natl. Acad. Sci. USA* **33**, 318–326.
- Warren, B. A.: 1981, *Deep circulation of the world ocean*, The MIT Press.
- Wicker, L. J. and Skamarock, W. C.: 1998, A Time-Splitting Scheme for the Elastic Equations Incorporating Second-Order Runge-Kutta Time Differencing, *Mon. Wea. Rev.* **126**, 1992–1999.

A Parameters of the Numerical Experiments, section 5

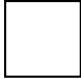
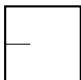
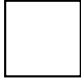
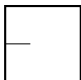
Restoring time of the upwelling	Shape of the basin	Injection type	$\nu = \kappa$ value ($\text{m}^2 \text{s}^{-1}$)	Age of the simulation	N°
$dt = 100$ or 200 s		Constant	1,000	20 years	A.1
			500	20 years	A.2
			250	20 years	A.3
			125	8 years	A.4
		1-yr periodical	1,000	20 years	B.1
			500	20 years	B.2
			250	20 years	B.3
			125	8 years	B.4
		Constant	1,000	20 years	C.1
			500	20 years	C.2
			250	20 years	C.3
			125	8 years	C.4
		1-yr periodical	1,000	16 years	D.1
			500	16 years	D.2
			250	16 years	D.3
			125	8 years	D.4
1 year		Constant	1,000	6 years	E.1
			500	6 years	E.2
			250	6 years	E.3
			125	4 years	E.4
		1-yr periodical	1,000	6 years	F.1
			500	6 years	F.2
			250	6 years	F.3
			125	4 years	F.4
		Constant	1,000	6 years	G.1
			500	6 years	G.2
			250	6 years	G.3
			125	4 years	G.4
		1-yr periodical	1,000	6 years	H.1
			500	6 years	H.2
			250	6 years	H.3
			125	4 years	H.4

Table 1: **Listing of the experiments. Every simulation is identified by its N°.** See the text section 5 for comments on the parameters. The different simulations were not started at the same time, and their achievement takes more or less time, this is why the final ages of the simulations are different. On average, it takes a little more time than one and a half day to perform a 1-year simulation.

B Illustrating Figures of the Section 6.4

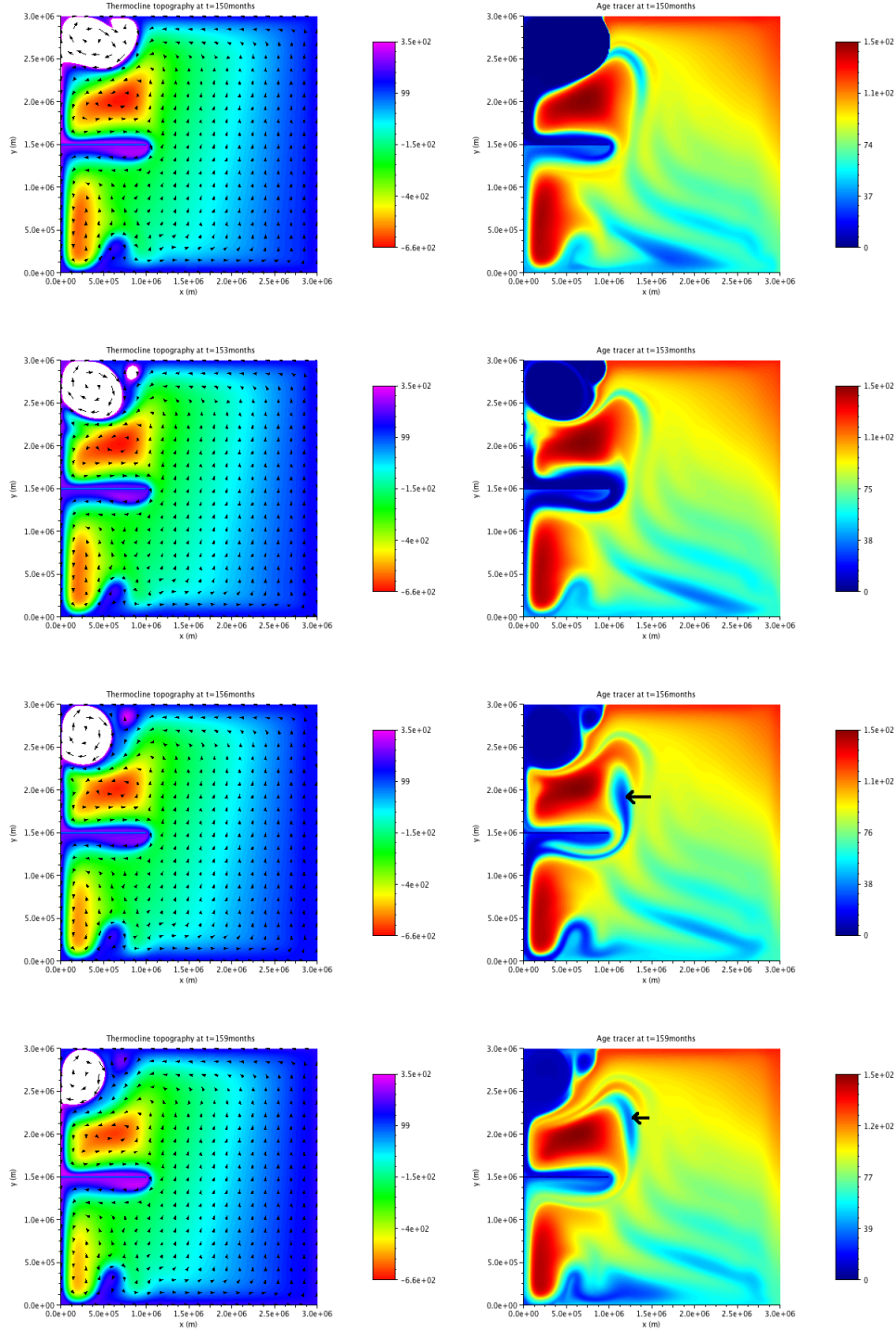


Figure 10: Above-views of the thermocline at $t=150, 153, 156$ and 159 months, in the D.3 simulation. Left panel: thermocline topography η . Right panel: age tracers A . The left color bar gives η values in m. In the non-painted zone, η is higher than 350 m. The right color bar gives A values in months. The obstacle is materialized by the zonal thin band at the western boundary, where $\eta = A = 0$. At $t = 150$ months, the injection (and the upwelling) is maximum. It decreases with time until the next year. The injection brings 0-years-old age tracers A . Black arrows show the structure of interest described in the text.